



Cite this: *J. Mater. Chem. C*, 2025, **13**, 2322

Jahn–Teller distortion induced two-dimensional ferroelasticity in Mn_2CuO_6 monolayers with antiferromagnetic ordering†

Xinkai Ding ^a and Gaoyang Gou ^{*b}

Designing and tuning Jahn–Teller (JT) distortion of two-dimensional (2D) materials plays a crucial role in multifunctional device applications, where significant 2D ferroelasticity in the crystal can be achieved by collaborative interactions among the spin, orbital and lattice degrees of freedom. Based on first-principles calculations, we report a Mn_2CuO_6 monolayer, a structural analogue derived from birnessite ($\delta\text{-MnO}_2$), as the material candidate for achieving JT distortion induced 2D ferroelasticity with antiferromagnetic (AFM) ordering. By performing electronic and magnetic property simulations as well as crystallographic symmetry analysis, we found that the ferroelastic (FE) deformation of the Mn_2CuO_6 monolayer is not only attributed to the structural phase transition, but also to JT distortion derived from the interplay among the electron spin, AFM ordering and crystal lattice, associated with metal–semiconductor and ferrimagnetic (FiM)–AFM transitions. The magnitude of FE strain in Mn_2CuO_6 monolayers is comparable with those of other typical 2D FE materials (e.g. 1T– MoS_2). The simulation of AFM–paramagnetic (PM) transition temperature ($T_N \sim 332$ K) for 2D FE in Mn_2CuO_6 further reveals the robust orbital orderings and room-temperature stable ferroelasticity. In addition, the FE switching among the three orientational variants is accompanied by the transformations of AFM spin textures, and a low transition barrier indicates that magnetic-tunable 2D lattice deformation can be readily achievable under experimental conditions, paving the way for the development of 2D magnetos-triction engineering for controllable electronic device applications.

Received 5th September 2024,
Accepted 25th November 2024

DOI: 10.1039/d4tc03801k

rsc.li/materials-c

1 Introduction

Perovskite manganite oxides have always attracted much attention for materials science research because of their unique electronic, magnetic and structural phase transition properties.^{1–3} Most research efforts, including cation doping^{4–6} and strain engineering,^{7–9} have been made to manipulate the metal–insulator and ferromagnetic (FM)–AFM phase transitions associated with JT distortion of perovskite manganite oxides, while the lattice degrees of freedom associated with the electronic or magnetic phase transition have long been overlooked. In fact, the experimentally detected spontaneous elastic strain in many 3D bulk crystals is typically lower than 0.2%,¹⁰ which can hardly receive experimental attention. In contrast, substantially larger lattice deformation is achievable for 2D van der Waals (vdW) layered materials, which has been validated in 2D materials such

as 1T– MoS_2 monolayers.¹¹ Moreover, previous research studies on 2D ferroics (ferroelasticity,^{12,13} ferromagnetism^{14,15} and ferroelectricity^{16,17}) indicate the feasibility for engineering the material properties and crystal structural phase transitions of 2D materials.¹⁸ Hence, JT distortion induced ferroelasticity, accompanied by the cooperative interplay among the spin, magnet and lattice degrees of freedom analogue to perovskite manganite oxides, can also be expected for 2D materials.

As a derivative of 2D layered $\delta\text{-MnO}_2$,^{19,20} 2D Mn_2CuO_6 can be synthesized by partial substitution of Mn by Cu cations, which have been realized for some 2D materials.^{21–23} Similar to $\delta\text{-MnO}_2$, the freestanding Mn_2CuO_6 monolayer possesses a layered perovskite structure with ordered arrangement of MnO_6 and CuO_6 octahedrons. Especially, JT distortion may occur in the Mn_2CuO_6 monolayer owing to e_g orbital ordering arising from Cu^{2+} JT ions, leading to JT ferroelasticity within the lattice. Similar examples can be found in some perovskite transition metal oxides^{24,25} and organic–inorganic hybrid compounds.²⁶ As illustrated in Fig. 1, the cooperative interplay among the spin, orbital and lattice degrees of freedom in the Mn_2CuO_6 monolayer can give rise to stable 2D ferroelasticity strongly dependent on magnetic configurations, which is desirable for realization of magnetic-tunable 2D lattice deformation, and

^a Department of Energy Materials and Chemical Engineering, Hefei University, Hefei 230601, People's Republic of China

^b Frontier Institute of Science and Technology, and State Key Laboratory of Electrical Insulation and Power Equipment, Xi'an Jiaotong University, Xi'an 710049, People's Republic of China. E-mail: gougayang@mail.xjtu.edu.cn

† Electronic supplementary information (ESI) available. See DOI: <https://doi.org/10.1039/d4tc03801k>

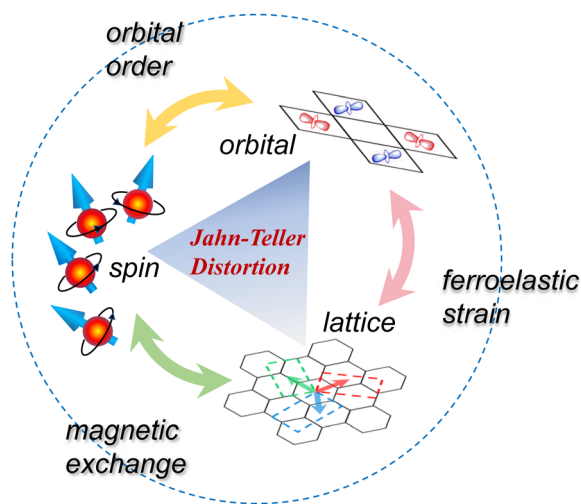


Fig. 1 Overview of 2D crystals with JT distortion. The competition of the various interactions listed around the circle indicates the rich interplay among the electron spin, orbital ordering and lattice deformation, as illustrated at the vertices of the triangle. These interplays in turn can lead to significant 2D ferroelasticity and stable magnetic orderings.

expected to develop 2D magnetostriction engineering for controllable electronic device applications.^{27,28}

In this work, based on first-principles calculations and Monte Carlo (MC) simulations, we demonstrate the Mn_2CuO_6 monolayer as a rare 2D FE material with JT distortion induced room-temperature stable 2D ferroelasticity and AFM ordering, which also exhibits magnetic-tunable 2D lattice deformation. We systematically simulate the crystal structures, magnetic configurations and electronic properties of the Mn_2CuO_6 monolayer. The interplay among the electron spin, orbital ordering and crystal lattice in the Mn_2CuO_6 monolayer leads to non-negligible 2D ferroelasticity, where its FE strain is far larger than that of 3D bulk materials,¹⁰ and is even comparable with that of typical 2D FE materials.²⁹ Moreover, the FE phase of the Mn_2CuO_6 monolayer has three equivalent orientational variants, and FE switching among three orientational variants can be driven by moderate mechanical strain. Next, based on the MC simulation, we predict an above room-temperature Neel temperature ($T_N \sim 332$ K) for the Mn_2CuO_6 monolayer, which indicates the room-temperature stable AFM ordering and 2D ferroelasticity. Finally, FE switching among three FE variants is also accompanied by the transformation of their magnetic spin textures. We thus propose a scheme for achieving magnetic controllable FE deformation within the Mn_2CuO_6 monolayer under experimental conditions.

2 Computational details

Our first-principles calculations are carried out based on density functional theory (DFT) as implemented in the Vienna *ab initio* simulation package (VASP),^{30–32} using the strongly constrained and appropriately normed (SCAN) *meta*-GGA functional,^{33,34} with the revised Vydrov–van Voorhis (rVV10) nonlocal correlation included.³⁵ A plane-wave basis set within the projector

augmented-wave (PAW) method is employed,³⁶ using a 650 eV plane-wave energy cutoff. Owing to the periodic boundary conditions required by first-principles plane wave calculations, the Mn_2CuO_6 monolayer is represented as a slab with a 20 Å vacuum region along the out-of-plane direction, ensuring periodic boundary conditions along the two in-plane directions. The Monkhorst–Pack *k*-point grids of $5 \times 9 \times 1$ and $5 \times 5 \times 1$ (~ 45 *k*-points per Å^{−1} spacing) are used to sample the 2D reciprocal lattice of FE and paraelastic (PE) Mn_2CuO_6 monolayers. A further increase of energy cut-off, *k*-point grid or vacuum spacing does not lead to an obvious change of the simulated energy or structural results. During the structural optimization, atomic positions and planar lattice parameters are fully optimized until the residual Hellmann–Feynman forces are smaller than 0.005 eV Å^{−1} and the stresses are less than 0.1 kbar. The Heyd–Scuseria–Ernzerhof hybrid functional (HSE06)³⁷ is used to simulate the electronic and magnetic properties of the Mn_2CuO_6 monolayer. Moreover, the spin–orbit coupling (SOC) is included during the simulations of magnetic anisotropy energy (MAE). In addition, the transition energy barrier between different orientation variants of the Mn_2CuO_6 monolayer has been evaluated by simulating the minimum energy path (MEP) trajectory using the generalized climbing image nudged elastic band (CI-NEB) method.^{38,39}

3 Results and discussion

3.1 Crystal structure and electronic spin

The Mn_2CuO_6 monolayer can be obtained by partial substitution of Mn by Cu cations in vdW layered $\delta\text{-MnO}_2$. As illustrated in Fig. 2(a), it contains three atomic layers, where the central atomic layers of Mn and Cu are coated with two outer O layers and form the edge-sharing MO_6 ($M = \text{Mn}$ or Cu) octahedral stacked nanosheets, and each CuO_6 octahedron is surrounded by six adjacent MnO_6 counterparts. According to our simulations, the FE Mn_2CuO_6 monolayer crystallizes in a distorted structural form with $C2/m$ symmetry, accompanied by a stripy-AFM (sAFM) spin texture. A metastable configuration adopted trigonal $P\bar{3}1m$ symmetry with the FiM1 spin texture can be used as the PE reference. As shown in Fig. 2(a), 2D crystallographic cells of FE and PE phases are marked in green and black colors, with $a = 8.587$ Å, $b = 4.907$ Å and $a_0 = 4.936$ Å, where the simulated energetic stabilities for two phases and their detailed crystallographic cell information are tabulated in Tables S1 and S2 of the ESI†. To confirm the stability of the FE phase structure, the phonon spectrum and *ab initio* molecular dynamics (MD) simulations are performed. No imaginary frequency appears in the whole Brillouin zones (Fig. S2 of ESI†), and no structural reconstruction or bond breaking occurs in the monolayer structure after performing *ab initio* MD simulations around 300 K up to 9 ps (Fig. S3 of the ESI†), indicating that the FE Mn_2CuO_6 monolayer with the sAFM spin texture is thermodynamically stable.

In order to investigate the underlying interplay between the crystal lattice and the electronic spin in FE and PE phases of the Mn_2CuO_6 monolayer, the electronic properties of both the PE and

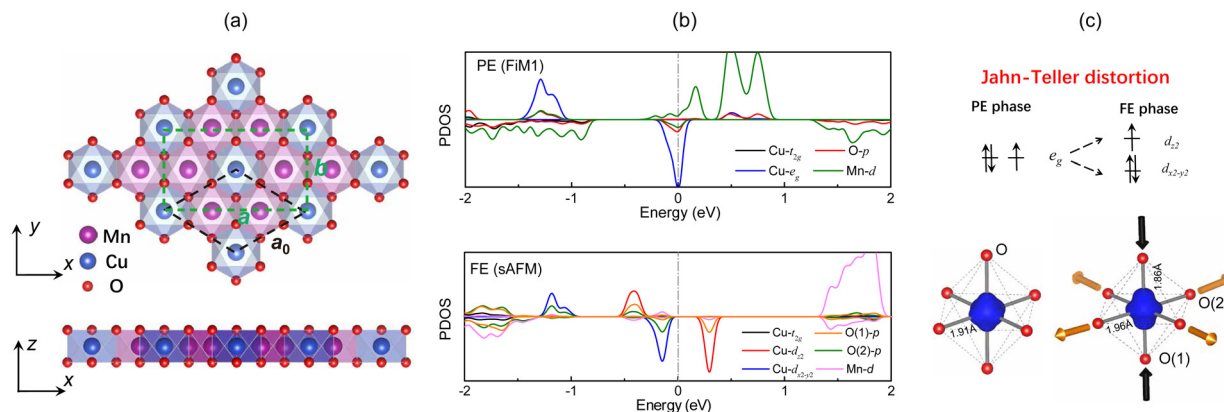


Fig. 2 (a) Top and side views of the atomic structure of the 2D Mn₂CuO₆ monolayer, where black dashed rhombus/green dashed rectangle denotes the crystallographic cell of the lattice without/with JT distortion. a_0 , a and b represent their lattice parameters. The orthogonal in-plane x and y axes are set along the directions of a and b . Blue and red polyhedrons are used to mark the structural CuO₆ and MnO₆ octahedrons, respectively. (b) The PDOS of the Mn₂CuO₆ monolayer with FiM1 and sAFM spin textures, where the Cu-3d orbital dominates electronic states around the Fermi level. The FiM–AFM magnetic phase transition is also accompanied by the metal–insulator electronic transition. (c) Illustrations of electronic spin configurations of Cu²⁺ ions in the crystal with and without JT distortion. Specifically, due to the Cu-*e_g* orbital splitting under the octahedral crystal field, apical O(1) of the CuO₆ octahedron is inequivalent to equatorial O(2), where Cu–O(1) bonds will be compressed and Cu–O(2) bonds will be elongated.

FE phase have been explored, and spin-polarized PDOS are plotted in Fig. 2(b). Our simulations indicate that the PE Mn₂CuO₆ monolayer exhibits metallic features, while the FE phase becomes insulated with a narrow band gap of 0.5 eV. According to our simulated spin-polarized PDOS, the energy bands around the Fermi level are composed predominately of the Cu-3d orbital in both PE and FE phases, where the Cu cation has the +2 valence state with the d⁹ valence–electron configuration. Owing to the octahedral CuO₆ crystal field, these d-orbitals can split into *e_g* (including *d_{x²−y²}* and *d_{z²}* orbitals) and *t_{2g}* parts, where the lower-energy *t_{2g}* orbitals fill with six valence electrons, and the rest three can distribute in *e_g* orbitals with the double degenerate states (*(d_{x²−y²}*)²(d_{z²)¹ and *(d_{x²−y²}*)¹(d_{z²)²). As a result, *e_g*-orbital-ordering of Cu²⁺ can break the degenerate states towards the lower-energy state by JT distortion and generates nonnegligible spontaneous FE strain in the lattice, leading to the anisotropic Cu–O bonds in the Mn₂CuO₆ monolayer Cu–O(1) and Cu–O(2), as illustrated in Fig. 2(c). More crystallographic information is summarized in Table S3 of the ESI.† Furthermore, we investigate some typical vibration modes of the CuO₆ octahedron and obtain their adiabatic potential energy profiles presented in Fig. S4 of the ESI.† Increasing the amplitude of vibration modes appropriately leads to the single well of potential energy profiles, which can generate spontaneous static JT distortion, driving the system to a stable low-symmetry state.}}

3.2 FE strain and variant energetics

Due to the octahedral CuO₆ structure and *P3̄1m* crystal symmetry of the PE phase, there are three symmetry-equivalent directions of JT distortion in PE–FE transition, where these directions are marked as colored arrows in Fig. 3(a) on the 2D rectangular shaded cells formed by Cu atoms. The relaxed atomistic structures associated with spin charge density distributions for the PE phase and three FE orientational variants with FiM1 and sAFM spin textures are shown in Fig. 3(b)–(d). Three orientational states of the FE phase are labelled as O1, O2

and O3, corresponding to the three directions of JT distortion. The non-zero spontaneous FE strain in the PE–FE transition of the Mn₂CuO₆ monolayer can be analyzed based on the 2 × 2 supercell of the parental PE phase. Specifically, we refer to the orthogonal in-plane x and y axes of the Cartesian coordinate as two diagonal directions of the parental PE phase. In this way, two basis vectors of the relaxed PE supercell shown in Fig. 3(b) can be written as $\vec{q}_1 = 2\sqrt{3}a_0\vec{x}$ and $\vec{q}_2 = 2a_0\vec{y}$, where \vec{x} and \vec{y} represent the unit vectors of x and y directions. A 2 × 2 structural matrix, $\mathbf{Q} = (\vec{q}_1, \vec{q}_2)$, is evaluated to represent in-plane lattice vectors for the PE phase as:

$$\mathbf{Q}_{\text{PE}} = \begin{pmatrix} 2\sqrt{3}a_0 & 0 \\ 0 & 2a_0 \end{pmatrix}. \quad (1)$$

Similarly, the planar lattice vectors of three FE orientational variants are labeled as the structural matrixes \mathbf{Q}_{O1} , \mathbf{Q}_{O2} and \mathbf{Q}_{O3} , respectively. The simulated equilibrium supercell matrixes of the 2D PE and FE Mn₂CuO₆ lattice are listed in Table S4 of the ESI.† According to these supercell matrixes, the 2D structural transformation strain matrixes η_i ($i = 1, 2$, and 3 denotes variants O1, O2 and O3, respectively) for PE–FE transition in the Mn₂CuO₆ monolayer can thus be calculated based on the definition of Green–Lagrange strain tensor as:

$$\eta_i = \frac{1}{2} \left[(\mathbf{Q}_{\text{PE}}^{-1})^T \mathbf{Q}_{\text{O}i}^T \mathbf{Q}_{\text{O}i} \mathbf{Q}_{\text{PE}}^{-1} - \mathbf{I} \right] \quad (2)$$

where the operations of matrix transposition and inversion are labelled with the superscripts T and ^{−1}, respectively. **I** represents the 2 × 2 identity matrix. This structural transformation strain matrix can have the following form:

$$\eta_i = \begin{pmatrix} \varepsilon_{xx} & \varepsilon_{xy} \\ \varepsilon_{xy} & \varepsilon_{yy} \end{pmatrix} \quad (3)$$

In eqn (3), ε_{xx} and ε_{yy} denote the axial strain along the two main axes and ε_{xy} is the shear strain. From our DFT calculations,

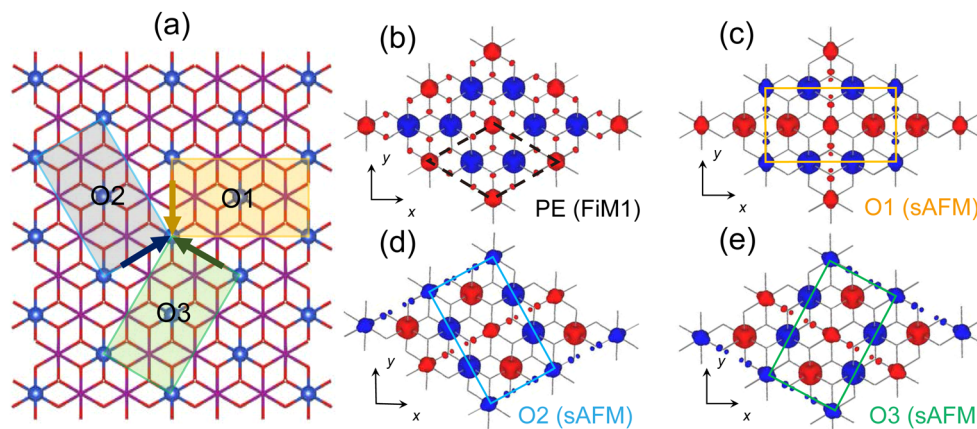


Fig. 3 Three orientational variants of the FE Mn_2CuO_6 monolayer. (a) O1, O2 and O3 FE variants originated from structural distortion of the hexagonal PE phase along three symmetry-equivalent directions, indicated by arrows and shaded triangular areas between neighboring Cu atoms. 2D crystallographic cells of variants O1, O2 and O3 are marked in yellow, blue and green colors, respectively. (b) The spin charge density distribution for the PE phase adopting the FiM1 spin texture in the 2×2 supercell, where its 2D crystallographic cell is marked as a black dash rhombus. (c)–(e) The spin charge density distributions of O1, O2 and O3 variants, where their 2D crystallographic cells are highlighted in yellow, blue and green boxes, respectively.

the results of 2D structural transformation strain matrices for the Mn_2CuO_6 monolayer are given as:

$$\begin{aligned} \eta_1 &= \begin{pmatrix} 0.47\% & 0 \\ 0 & -0.57\% \end{pmatrix}, \\ \eta_2 &= \begin{pmatrix} -0.32\% & -0.44\% \\ -0.44\% & 0.21\% \end{pmatrix}, \\ \eta_3 &= \begin{pmatrix} -0.32\% & 0.44\% \\ 0.44\% & 0.21\% \end{pmatrix}. \end{aligned} \quad (4)$$

The difference among η_1 , η_2 and η_3 provides the possibility of FE switching among the three equivalent orientational variants driven by external mechanical strains, and our calculated supercell structures of these three FE variants originate from the same parental PE phase. Owing to the zero shear strain in η_1 , we thus take variant O1 as a reference state, and the relative transformation strain matrices of the structural transition from one variant to another can be directly computed based on eqn (2). Transformation strain tensors during FE switching from variant O1 to O2 or O1 to O3 are written as:

$$\begin{aligned} \eta_1^2 &= \begin{pmatrix} -0.77\% & -0.44\% \\ -0.44\% & 0.78\% \end{pmatrix}, \\ \eta_1^3 &= \begin{pmatrix} -0.77\% & 0.44\% \\ 0.44\% & 0.78\% \end{pmatrix}. \end{aligned} \quad (5)$$

In this way, FE switching from variant O1 to O2 (O3) can be availably realized by applying external mechanical strain of magnitude η_1^2 (η_1^3) in the monolayer.

To further analyze the relative thermodynamic stability among the three orientational variants under external strains, we first consider the possibility of FE variant switching from O1 to O2 (or O3) under biaxial strain. Taking the relaxed 2D

supercell of variant O1 as the reference, we plot the potential energy surfaces of the three variants as a function of the planar normal strain rate, where the two diagonal lines of the O1 supercell perpendicular to each other exactly extend along a (x axis) and b (y axis) directions, respectively. The dimensions of the supercell are independently adjusted along a and b directions by equably applying mechanical strain within the range from -6 to 6% at a step of 0.5% . Each pair of the axial normal strain is imposed on the lattice and corresponds to one point of 2D potential energy surfaces, where the atomic coordinates of the calculated configuration are fully relaxed. The free energies of variants O2 and O3 and the PE phase with the corresponding magnetic spin texture are then computed based on the aforementioned O1 supercells with the fixed lattice dimensions.

Our calculated results are summarized on a 25×25 grid of the 2D (a, b) plane, distributed around the equilibrium lattice parameters of variant O1. The intersection contours of potential energy surfaces $U(a, b)$ among the PE phase and the three FE orientational variants can be obtained by using quadratic spline interpolation. Based on the full (a, b) diagram illustrated in Fig. 4(a), we can visually compare the relative thermodynamic stability of the three orientational variants and the PE phase under external strain, where we label the thermodynamically favourable variant/phase in each phase-space region and draw the intersection boundaries between the two adjacent variants/phases. In Fig. 4(a), a distinct feature is that variants O2 and O3 share the same region of the phase space, indicating energetically degenerate states under external biaxial strains, and can be attributed to the fact that their lattice distortions from the parental PE phase are always mirror images of each other along the y axis, while the homogeneous biaxial normal strain cannot break this energy-degeneracy state. As illustrated in Fig. 4(b), when we apply a shear strain ϵ_{xy} with a magnitude larger than 1% to the variant O1, the most thermodynamically stable variant will change to O2. If ϵ_{xy} is the negative number, the variant O3 will have the lowest energy. In this way,

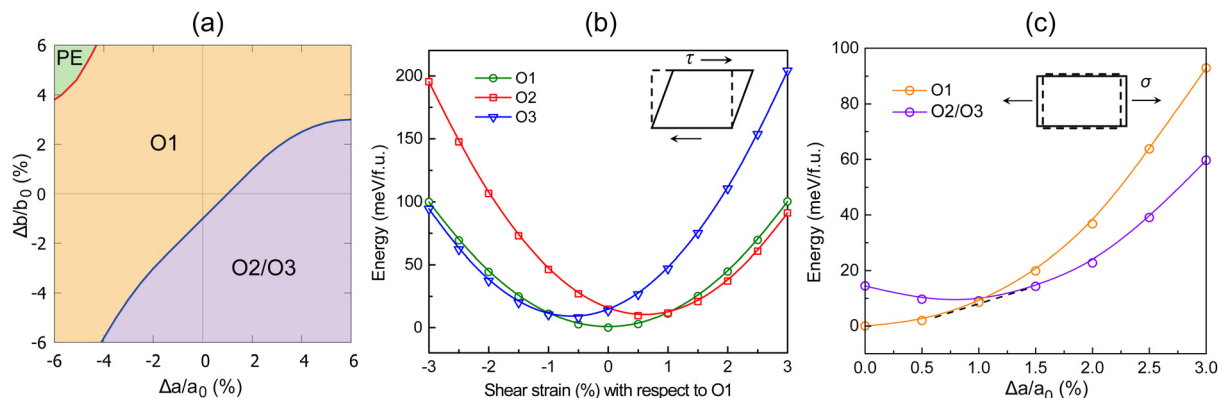


Fig. 4 FE phase transition and energetics under mechanical strains. (a) The energy interpolating contours of the Mn_2CuO_6 monolayer between PE and FE (including O1, O2 and O3 orientational variants). $\Delta a/a_0$ and $\Delta b/b_0$ represent the axial strain relative to the equilibrium lattice constants of the 2D rectangular crystallographic cell for variant O1. The lowest energy variant/phase regions are labelled or shaded in different colors. The energy profiles of three orientational variants of the Mn_2CuO_6 monolayer as a function of (b) shear and (c) uniaxial tension strains. When imposing the shear strain on variant O1, transition into variant O2/O3 with lower energy will occur. The common tangent between O1 and O2/O3 curves is drawn as a dashed line. By applying a uniaxial tension strain along the a direction of variant O1 (x axis), variant O2/O3 will become thermodynamically more favorable, where the multiple variants will coexist within the range of the tangent line.

variants O2 and O3 are no longer degenerate in energy, and all the three FE variants can be well classified.

Moreover, according to our simulations, the FE variant switching from variant O1 to O2/O3 can be directly realized by imposing tensile strain along the a direction or compressive strain along the b direction on the lattice. Due to the edge compression-bending response reported in some 2D layered materials with surface ripplocations under compressive strain,⁴⁰ we only consider the tension of the monolayer and plot potential energy profiles (Fig. 4(c)) as a function of uniaxial tensile strain along the a direction, which is perpendicular to the direction of JT distortion in the lattice. The variant O2/O3 holds the same dimension of the variant O1 and zero strain is ensured along the b direction ($\sigma_y = 0$). Because of the negligible entropy change of Mn_2CuO_6 solids under ambient conditions ($\Delta S \approx 0$), it is rational to substitute the Helmholtz free energy ($A = E - T\Delta S$) with the potential energy of the system, and a common tangent with the crossing points being 0.7% and 1.5% can be drawn between the curves of variants O1 and O2/O3. As a result, the system prefers to variant coexistence when the uniaxial strain $\Delta a/a_0$ falls within the range of the two values.

3.3 AFM ordering and magnetic-tunable FE variant switching

So far, we have demonstrated the phenomenon of spontaneous FE variant switching and their thermodynamics in the Mn_2CuO_6 monolayer. Its lattice deformation is mainly attributed to JT distortion derived from the d-orbital ordering of Cu^{2+} ions. Moreover, this d-orbital ordering can be accompanied by magnetic ordering in the monolayer, leading to the sAFM spin texture of the magnetic ordering. Namely, the cooperative interplay between AFM ordering and the crystal lattice can affect 2D ferroelasticity in the Mn_2CuO_6 monolayer. When the magnetic state evolves towards the disordered PM state with the high ambient temperature, the spontaneous FE-PE transition associated with absent JT distortion can be expected. Hence, research on the magnetic

properties of the Mn_2CuO_6 monolayer and the interplay between FE deformation and magnetic ordering is thus necessary. To determine the easy axis of the magnetic moment, we perform the magnetic anisotropy energy (MAE) calculations as follows:

$$\text{MAE} = \frac{E_{[hkl]} - E_{[001]}}{N} \quad (6)$$

where $E_{[hkl]}$ and $E_{[001]}$ denote the total energy along the $[hkl]$ and $[001]$ directions, respectively and N is the number of the cations (Cu and Mn) in the unit cell. We simulate MAE to evaluate the orientation of magnetic easy axis⁴¹ for achieving long-range magnetic ordering, and it should include the SOC effect. The angle dependence of the simulated MAE is plotted in Fig. 5(a), and the specific values of major magnetization directions are listed in Table S5 of the ESI.† According to our DFT calculations, all the values of MAE are positive, indicating an out-of-plane magnetic easy axis in the Mn_2CuO_6 monolayer. Comparing with the in-plane direction, the significant changes of the MAE appear on the out-of-plane direction, similar to most of the 2D magnetic materials.^{42–44}

Owing to the cooperative interplay between the FE-PE structural transition and the sAFM-PM magnetic transition in the Mn_2CuO_6 monolayer, it is reasonable that the higher magnetic transition temperature of the monolayer can be anticipated for the better temperature adaptability of the FE phase. Utilizing the vectorized magnetic moments of cations in the Mn_2CuO_6 monolayer, we can estimate the T_N of the system based on the Heisenberg spin Hamiltonian defined as:

$$\hat{H} = - \sum_{i \neq j} J_{1\xi} \vec{S}_i \cdot \vec{S}_j - \sum_{i \neq k} J_{2\xi} \vec{S}_i \cdot \vec{S}_k \quad (7)$$

where \vec{S}_i , \vec{S}_j , and \vec{S}_k denote the unit vectors of local spin moment at i , j , and k sites. In our simulations, the $|\vec{S}|$ s of Cu and Mn cations in high-spin states are set as 1/2 and 1, respectively. $J_{1\xi}$ and $J_{2\xi}$ are the nearest-neighbor and next-nearest-neighbor

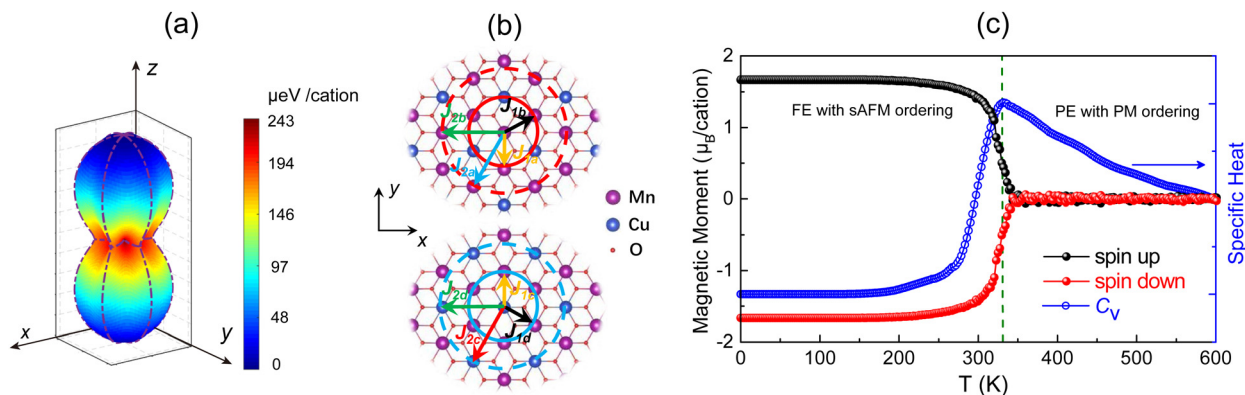


Fig. 5 The magnetic properties of the Mn_2CuO_6 monolayer. (a) The 3D angle-dependent magnetic anisotropic energy (MAE) of the FE Mn_2CuO_6 monolayer. The magnetic easy axis is along the out-of-plane direction. (b) Schematic representations of the nearest-neighbor ($J_{1\xi}$) and next-nearest-neighbor ($J_{2\xi}$) exchange interactions between Mn and Cu cations. Due to JT distortion induced lattice deformation and two distinct magnetic cations in the 2D Mn_2CuO_6 crystal, label subscript $\xi = a, b, c$ or d is adopted to distinguish inequivalent magnetic exchange parameters. (c) MC simulation of temperature-dependent normalized magnetic moments for the FE Mn_2CuO_6 monolayer, where magnetic moments from the inequivalent spin lattice grids are indicated as black and red circles. Our simulated temperature dependent specific heat C_v is indicated by a blue circle, and a T_N up to 332 K appears at a peak position of C_v . When the temperature is above T_N , the FE–PE transition occurs in the Mn_2CuO_6 monolayer accompanied by sAFM–PM magnetic transition.

exchange interaction parameters, and each $J_{1\xi}$ or $J_{2\xi}$ can be varied depending on JT distortion and the magnetic cations in the crystal. These inequivalent exchange interaction parameters are differentiated with the subscript ξ ($\xi = a, b, c$ or d , illustrated in Fig. 5(b)), which can be obtained by using eqn (7) (Table S6 of the ESI†).

According to our calculations, the magnetic exchange interactions in the crystal mainly occur between the Cu and Mn cations ($J_{1c} = 37.01$ meV and $J_{1d} = -52.20$ meV), where the positive or negative sign denotes the FM or AFM coupling. Besides, the half-occupied Cu- d_{z^2} orbitals partially hybridize with O-p orbitals and dominate at the Fermi level, associated with the low chemical potential and active electronic states. On the other hand, the highly-charged Mn^{5+} in Mn_2CuO_6 monolayer can perform strongly oxidizing features. Based on Goodenough–Kanamori–Anderson rules,^{45–47} on the direction of half-occupied Cu- d_{z^2} orbitals, an O-mediated strong super-exchange interaction could form, where the participant electron spins prefer to antiparallel alignments,⁴⁸ leading to AFM couplings between the central Cu and adjacent four Mn cations. Meanwhile, in the direction perpendicular to the half-occupied Cu- d_{z^2} orbitals, the super-exchange interaction could exist between the single electron spin of Cu^{2+} and empty orbitals of Mn^{5+} , leading to FM couplings between the central Cu and the other two neighboring Mn cations. Comparing with the FM couplings, the more sufficient orbital overlap of AFM couplings makes the larger magnitude of the J_{1d} .

Utilizing MC simulations, we construct a 2D Ising model of the 200×300 supercell including total 60 000 local magnetic sites to quantitatively estimate the Néel temperature T_N of the system. In our MC calculations, we construct the simulated model under periodic boundary conditions and operate 6×10^8 loops in each temperature step of 1 K. When the critical temperature T_N is reached, the temperature-dependent specific heat C_v , defined as $C_v = \frac{\langle E^2 \rangle - \langle E \rangle^2}{k_B T^2}$, will reach the extreme

value point. As illustrated in Fig. 5(c), the spin-up and spin-down curves converge into the zero at the peak position of specific heat C_v , with a T_N of 332 K. To confirm the reliability of this critical temperature, the MC simulations for the two typical AFM perovskite oxides, BiFeO_3 and $\text{CaMnTi}_2\text{O}_6$, are performed by the use of the same approach, where our simulated T_N s are around 675 K for BiFeO_3 and 14.8 K for $\text{CaMnTi}_2\text{O}_6$ (Fig. S5 of the ESI†), close to the experimental measurements of 643 K (ref. 49) and 10 K,⁵⁰ respectively. Therefore, our simulated T_N of the Mn_2CuO_6 monolayer is reliable. Once the ambient temperature increases over the T_N , AFM ordering in materials will vanish and the associated FE–PE phase transition can be thus predicted. It should be noted that our simulated T_N of the Mn_2CuO_6 monolayer is higher than room temperature (300 K), namely, the stability of the room-temperature FE phase accompanied by orbital ordering in the Mn_2CuO_6 monolayer can be confirmed.

Since the stable 2D ferroelasticity of the Mn_2CuO_6 monolayer is strongly dependent on magnetic configurations, it is desirable for realization of FE switching among three orientational variants by the transformations of magnetic spin textures. As shown in Fig. 6(a), to evaluate the possibility of the scheme, we take O1–O2 FE variant switching as an example. The kinetic energy barriers, with three fixed magnetic textures (including sAFM-O1, sAFM-O2 and FiM1), are calculated, where the MEP trajectory is plotted in Fig. 6(b). According to our calculation, the intermediate state with the FiM1 spin texture can facilitate variants O1 and O2 with a kinetic energy barrier of 94.7 meV f.u.^{−1}, which is lower than the barrier of the individual two AFM curves. This value is larger than the FE transition barrier of the GeSe monolayer (10 meV f.u.^{−1}),¹⁷ but smaller than that of the WTe_2 monolayer (190 meV f.u.^{−1}).²⁹ Therefore, the FE switching of the Mn_2CuO_6 monolayer can be realized by means of the intermediate PE phase with the FiM1 spin texture. The low barrier of the FE–PE–FE transition indicates that magnetic-tunable 2D lattice deformation, even 2D magnetostriction

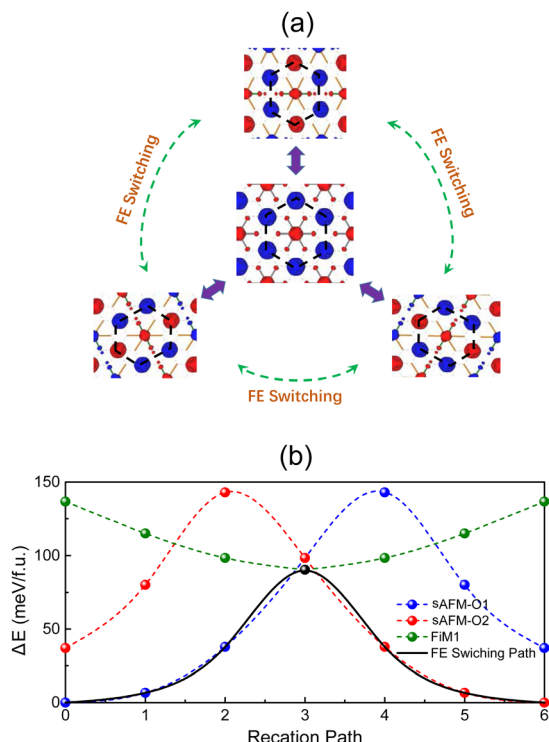


Fig. 6 (a) A schematic diagram of magnetic-tunable FE variant switching within the Mn_2CuO_6 monolayer. (b) The kinetic energy barrier for O1–O2 FE variant switching is assisted by the FiM1 spin texture. Kinetic reaction paths from the variant O1 to O2 with three different magnetic orderings (sAFM–O1, sAFM–O2 and FiM1) are under simulations, where the corresponding energy pathways are in blue, red and green colors, respectively. The FiM1 spin texture can facilitate O1–O2 FE variant switching with a lower kinetic energy barrier, and the corresponding kinetic reaction path is shown as a black curve.

engineering, can be readily achievable under experimental conditions.

4 Conclusions

In summary, based on the first-principles calculations and MC simulations, we systematically demonstrated the Mn_2CuO_6 monolayer, a structural derivative of the layered $\delta\text{-MnO}_2$, which characterizes JT-distortion-induced 2D ferroelasticity with sAFM magnetic ordering. Specifically, intrinsic 2D ferroelasticity in the Mn_2CuO_6 monolayer is not only attributed to a simple structural phase transition, but also to the cooperative interplay among lattice deformation, magnetic exchange and orbital ordering of Cu^{2+} ions. Especially, the magnitude of FE strain harbored by the Mn_2CuO_6 monolayer can overwhelm the 3D Perovskite magnetite bulk. FE switching kinetics of the Mn_2CuO_6 monolayer under mechanical deformation is also under simulations, where a moderate mechanical strain can trigger the switching among three inequivalent orientational variants. Using MC simulations, a T_N up to 332 K is predicted for the FE Mn_2CuO_6 monolayer, which indicates the room-temperature stable 2D ferroelasticity associated with the stable AFM magnetic ordering in the Mn_2CuO_6 monolayer. Finally, based on the

simulated switching pathway, we propose a feasible scheme for realizing the magnetic-tunable FE switching, and even 2D magnetostriction engineering in 2D Mn_2CuO_6 , awaiting experimental realization.

Author contributions

The authors' contributions are described as below. Xinkai Ding: investigation, software, data curation, formal analysis, writing – original draft, and funding acquisition. Gaoyang Gou: conceptualization, resources, supervision, writing – review and editing, and funding acquisition.

Data availability

The authors confirm that the data supporting the findings of this study are available within the article and the ESI.†

Conflicts of interest

There are no conflicts to declare.

Acknowledgements

The authors acknowledge the funding support from the National Natural Science Foundation of China (Grant No. 11574244 and No. 52075144), the Fundamental Research Funds for the Central Universities (xzy012020004), the Natural Science Research Project for Anhui Universities (2024AH051519), the Talent Scientific Research Foundation of Hefei University (23RC31), the State Key Laboratory for Mechanical Behavior of Materials (20212302), and the Excellent Scientific Research and Innovation Team of Anhui Universities (2022AH010096). Hefei Advanced Computing Center is acknowledged for computational support.

Notes and references

- 1 J. Cong, K. Zhai, Y. Chai, D. Shang, D. D. Khalyavin, R. D. Johnson, D. P. Kozlenko, S. E. Kichanov, A. M. Abakumov, A. A. Tsirlin, L. Dubrovinsky, X. Xu, Z. Sheng, S. V. Ovsyannikov and Y. Sun, *Nat. Commun.*, 2018, **9**, 2996.
- 2 Z. Gai, W. Lin, J. D. Burton, K. Fuchigami, P. C. Snijders, T. Z. Ward, E. Y. Tsymbal, J. Shen, S. Jesse, S. V. Kalinin and A. P. Baddorf, *Nat. Commun.*, 2014, **5**, 4528.
- 3 M. Tachibana, T. Shimoyama, H. Kawaji, T. Atake and E. Takayama-Muromachi, *Phys. Rev. B:Condens. Matter Mater. Phys.*, 2007, **75**, 144425.
- 4 A. Bandyopadhyay, S. Li and T. Frauenheim, *J. Phys. Chem. Lett.*, 2022, **13**, 6755–6761.
- 5 E. Liu and D. Higgins, *Nat. Catal.*, 2024, **7**, 469–471.
- 6 X. Zhu, S. Jin, X. Yu, Z. Yu, X. Gu, X. Guan, K. Wu, Y. Yan, L. Zhao, J. Han, J. Jiang, X. Liu and X. Li, *Appl. Surf. Sci.*, 2023, **630**, 157511.
- 7 Y. H. Chang, A. Pal, P. T. W. Yen, C. W. Wang, S. Giri, G. R. Blake, J. Gainza, M.-J. Hsieh, J.-Y. Lin, C. Y. Huang,

- Y. J. Chen, T. W. Kuo, A. Tiwari, D. Chandrasekhar Kakarla and H. D. Yang, *Phys. Rev. B*, 2024, **110**, 064405.
- 8 Y. Zhang, P. Han, M. P. K. Sahoo, X. He, J. Wang and P. Ghosez, *Phys. Rev. B*, 2022, **106**, 235156.
- 9 X. Chen, Z. Wan, Z. Zhou, X. Luo and D. Xu, *J. Energy Storage*, 2024, **94**, 112498.
- 10 W. Li, X. Qian and J. Li, *Nat. Rev. Mater.*, 2021, **6**, 829–846.
- 11 S. Bertolazzi, J. Brivio and A. Kis, *ACS Nano*, 2011, **5**, 9703–9709.
- 12 X. Ding, Y. Jia and G. Gou, *J. Phys. Chem. Lett.*, 2023, **14**, 420–429.
- 13 X. Xuan, W. Guo and Z. Zhang, *Phys. Rev. Lett.*, 2022, **129**, 047602.
- 14 S. Lu, Q. Zhou, Y. Guo, Y. Zhang, Y. Wu and J. Wang, *Adv. Mater.*, 2020, **32**, 2002658.
- 15 M. A. Rahman, J. P. Thomas, M. Beedel, X. Guan, N. F. Heinig, L. Zhang and K. T. Leung, *J. Mater. Chem. C*, 2023, **11**, 9837–9849.
- 16 X. Chen, X. Ding, G. Gou and X. C. Zeng, *Nano Lett.*, 2024, **24**, 3089–3096.
- 17 H. Wang and X. Qian, *2D Mater.*, 2017, **4**, 015042.
- 18 S. Barraza-Lopez, B. M. Fregoso, J. W. Villanova, S. S. P. Parkin and K. Chang, *Rev. Mod. Phys.*, 2021, **93**, 011001.
- 19 W. Cheng, J. Lindholm, M. Holmboe, N. T. Luong, A. Shchukarev, E. S. Ilton, K. Hanna and J. F. Boily, *Langmuir*, 2021, **37**, 666–674.
- 20 J. E. Post, *Proc. Natl. Acad. Sci. U. S. A.*, 1999, **96**, 3447–3454.
- 21 Y. C. Lin, R. Torsi, D. B. Geohegan, J. A. Robinson and K. Xiao, *Adv. Sci.*, 2021, **8**, 2004249.
- 22 A. M. Makarevich, I. I. Sadykov, D. I. Sharovarov, V. A. Amelichev, A. A. Adamenkov, D. M. Tsybarenko, A. V. Plokhii, M. N. Esaulkov, P. M. Solyankin and A. R. Kaul, *J. Mater. Chem. C*, 2015, **3**, 9197–9205.
- 23 A. Bandyopadhyay, N. C. Frey, D. Jariwala and V. B. Shenoy, *Nano Lett.*, 2019, **19**, 7793–7800.
- 24 Y.-J. Kim, H.-S. Park and C.-H. Yang, *npj Quantum Mater.*, 2021, **6**, 62.
- 25 Q. Zhou and B. J. Kennedy, *J. Phys. Chem. Solids*, 2007, **68**, 1643–1647.
- 26 S.-Q. Yin, Y.-Q. Tong, Q.-J. Gu, Y.-J. Li, B. Huang and A.-X. Zhu, *J. Mater. Chem. C*, 2024, **12**, 7862–7866.
- 27 H. Y. Huang, Z. Y. Chen, R. P. Wang, F. M. F. d Groot, W. B. Wu, J. Okamoto, A. Chainani, A. Singh, Z. Y. Li, J. S. Zhou, H. T. Jeng, G. Y. Guo, J. Park, L. H. Tjeng, C. T. Chen and D. J. Huang, *Nat. Commun.*, 2017, **8**, 15929.
- 28 K. Ji, Z. Wu, X. Shen, J. Wang and J. Zhang, *Phys. Rev. B*, 2023, **107**, 134431.
- 29 W. Li and J. Li, *Nat. Commun.*, 2016, **7**, 10843.
- 30 G. Kresse and J. Hafner, *Phys. Rev. B:Condens. Matter Mater. Phys.*, 1993, **48**, 13115–13118.
- 31 G. Kresse and J. Furthmuller, *Comput. Mater. Sci.*, 1996, **6**, 15–50.
- 32 G. Kresse and J. Furthmuller, *Phys. Rev. B:Condens. Matter Mater. Phys.*, 1996, **54**, 11169–11186.
- 33 J. Sun, A. Ruzsinszky and J. P. Perdew, *Phys. Rev. Lett.*, 2015, **115**, 036402.
- 34 J. Sun, R. C. Remsing, Y. Zhang, Z. Sun, A. Ruzsinszky, H. Peng, Z. Yang, A. Paul, U. V. Waghmare, X. Wu, M. L. Klein and J. P. Perdew, *Nat. Chem.*, 2016, **8**, 831–836.
- 35 H. Peng, Z. Yang, J. P. Perdew and J. Sun, *Phys. Rev. X*, 2016, **6**, 041005.
- 36 P. E. Blochl, *Phys. Rev. B:Condens. Matter Mater. Phys.*, 1994, **50**, 17953–17979.
- 37 J. Heyd, G. E. Scuseria and M. Ernzerhof, *J. Chem. Phys.*, 2003, **118**, 8207–8215.
- 38 G. Henkelman, B. P. Uberuaga and H. Jonsson, *J. Chem. Phys.*, 2000, **113**, 9901–9904.
- 39 G. Henkelman and H. Jonsson, *J. Chem. Phys.*, 2000, **113**, 9978–9985.
- 40 A. Kushima, X. Qian, P. Zhao, S. Zhang and J. Li, *Nano Lett.*, 2015, **15**, 1302–1308.
- 41 N. D. Mermin and H. Wagner, *Phys. Rev. Lett.*, 1966, **17**, 1133–1136.
- 42 S. Xing, J. Zhou, X. Zhang, S. Elliott and Z. Sun, *Prog. Mater. Sci.*, 2023, **132**, 101036.
- 43 S. Wang, N. Miao, K. Su, V. A. Blatov and J. Wang, *Nanoscale*, 2021, **13**, 8254–8263.
- 44 K. F. Mak, J. Shan and D. C. Ralph, *Nat. Rev. Phys.*, 2019, **1**, 646–661.
- 45 J. Kanamori, *J. Appl. Phys.*, 1960, **31**, S14–S23.
- 46 P. W. Anderson, *Phys. Rev.*, 1959, **115**, 2–13.
- 47 J. B. Goodenough, *Phys. Rev.*, 1955, **100**, 564–573.
- 48 L. Zhang, C. Tang and A. Du, *J. Mater. Chem. C*, 2021, **9**, 95–100.
- 49 R. Zhang, H. Dong, M. Wen and F. Wu, *Inorg. Chem.*, 2023, **62**, 16059–16067.
- 50 A. Aimi, D. Mori, K.-i Hiraki, T. Takahashi, Y. J. Shan, Y. Shirako, J. Zhou and Y. Inaguma, *Chem. Mater.*, 2014, **26**, 2601–2608.